Acta Materialia 257 (2023) 119182

Contents lists available at ScienceDirect

Acta Materialia

journal homepage: www.elsevier.com/locate/actamat

Full length article

Heterostructures enhance simultaneously strength and ductility of a commercial titanium alloy

Di Wu [a,c,1], Mengyuan Hao [b,1], Tianlong Zhang [b,e,f,1], Zhen Wang [c], Jiang Wang [c], Guanghui Rao [c], Ligang Zhang [a], Chaoyi Ding [a], Kechao Zhou [a], Libin Liu [a,*], Dong Wang [b,*], Yunzhi Wang [d,*]

[a] School of Material Science and Engineering, State Key Laboratory of Powder Metallurgy, Central South University, Changsha, Hunan 410083, China
[b] Center of Microstructure science, Frontier Institute of Science and Technology, State Key Laboratory for Mechanical Behavior of Materials, Xi'an Jiaotong University, Xi'an 710049, China
[c] School of Materials Science and Engineering, Guangxi Key Laboratory of Information Materials, Guilin University of Electronic Technology, Guilin 541004, China
[d] Department of Materials Science and Engineering, The Ohio State University, Columbus, OH 43210, United States
[e] Department of Materials Science and Engineering, Hong Kong Institute for Advanced Study, College of Science and Engineering, City University of Hong Kong, Hong Kong 999077, China
[f] Department of Mechanical and Aerospace Engineering, The Hong Kong University of Science and Technology, Clear Water Bay, Kowloon, Hong Kong, China

ARTICLE INFO

Keywords:
Metastable β titanium alloy
Heat treatment
Precipitation
Pseudo-spinodal decomposition
Strength and ductility

ABSTRACT

Enhancing both strength and ductility simultaneously in commercial alloys at an industrial scale remains a challenging task. In this study, we have demonstrated a simple heat treatment method to achieve a heterostructure with coarse and ultra-fine lamellar α precipitates in a common titanium alloy, Ti-5Al-5Mo-5V-3Cr-1Zr. Guided by computer simulations, we successfully attained microscale concentration modulations in the β-phase matrix using up-quenching of a duplex microstructure consisting of a globular primary α phase (α_p) and β matrix to dissolve the α_p phase rapidly and leave residual concentrations. We subsequently applied aging treatments to create finely dispersed regions of coarse and ultra-fine α precipitates embedded in the β matrix by activating different phase transformation mechanisms. Compared to the commercial alloy that has a homogeneous lamellar structure, the heterostructured alloy we produced exhibits a 6% increase in ultimate tensile strength and a remarkable 130% increase in elongation. The outstanding ductility of the heterostructured alloy is attributable to its unique microstructure design, which prevents strain localization and allows full activation of dislocation and twin deformations in the coarse and ultra-fine α regions. Meanwhile, the high strength of the alloy can be attributed to the enhanced back stress effect induced by strain partitioning of the heterostructure. Our study demonstrates a simple and effective method for creating bulk heterostructures in precipitation-hardened alloys at an industrial scale, leading to substantially improved strength and ductility.

1. Introduction

The design of alloys with a synergistic combination of strength and ductility is still a daunting challenge to the materials science and engineering community [1–3]. In recent years, heterostructured materials, defined as materials composed of regions with significantly different physical and mechanical properties, have attracted much attention [4]. Its ability to obtain superior mechanical properties by the ordered superposition of these different property regions (Such as soft plastic coarse grains and hard ultra-fine nano-grains), the comprehensive performance exceeds the prediction of the rule of mixtures [5,6]. These superior mechanical properties are mainly based on the synergistic strengthening effect between the different regions, i.e., hetero-deformation induced strengthening and work hardening. Specifically, under tensile loading, the soft region of the coarse grains deforms preferentially, and dislocations accumulate and form strain gradients at the interface (the interface between the soft and hard regions) due to being confined by the surrounding hard region [7,8]. The

* Corresponding authors.
E-mail addresses: lbliu@csu.edu.cn (L. Liu), wang_dong1223@mail.xjtu.edu.cn (D. Wang), wang.363@osu.edu (Y. Wang).
[1] They are co-first authors because they all implemented the experimental or simulation part.

https://doi.org/10.1016/j.actamat.2023.119182
Received 18 April 2023; Received in revised form 30 June 2023; Accepted 22 July 2023
Available online 22 July 2023

strain gradient from hetero-deformation will generate back stresses in the soft region and forward stresses in the hard zone. The generation of back stresses will contribute to the strengthening of the soft region, while the forward stresses contribute to the yielding and deformation of the hard region, which will contribute to the strength and ductility of the alloy, respectively. Clearly, the size, geometry and distribution of the heterogeneous regions will be key to the properties of the alloy, yet it is not easy to design customized and controlled combinations of heterogeneous regions, which usually involve elaborate preparation and processing approaches. For example, various heterostructures such as gradient structures with different grain sizes [9], heterogeneously layered structures [10], nanoscale solute undulation [11,12] and harmonic structures [13,14] have been created in recent years by using various innovative processing techniques, including surface grinding treatments [9], multi-pass asymmetric rolling [10], pulsed electrodeposition [11] and spark plasma sintering [13]. However, these sophisticated processing methods are either limited to small scale laboratory demonstrations or being able to produce heterostructured specimens only in micron-scale, and difficult or impractical to be realized in large-scale commercial manufacturing of bulk heterostructured alloys [15,16].

In this study, we demonstrate a simple and efficient method to fabricate heterostructure in a commercial titanium alloy, Ti-5Al-5Mo-5V-3Cr-1Zr (Ti-55531, in weight percent), which is a high-strength titanium alloy used in landing gears of Boeing-787 and Airbus-380 airliners [17–21]. Guided by phase field microstructural simulations, heterostructured alloys with coarse and ultra-fine lamellar α precipitates are designed and successfully fabricated by using a simple three-step heat treatment. We first produce a duplex microstructure consisting of globular primary α (α_p) precipitates + β matrix by annealing a forged alloy in the α + β two-phase region of the phase diagram. We then up-quench the alloy to above the β-transus and isothermally hold for a short period of time to dissolve the α_p precipitates structurally but do not allow the solutes to homogenize, producing α stabilizer rich and α stabilizer lean regions. We finally bring this compositionally modulated single phase β back into the α + β two phase region to activate both the nucleation-and-growth mechanism and the congruent structural transformation mechanism for lamellar α precipitation during isothermal holding. Compared with the conventional alloy having homogeneous lamellar structures, our heterostructured alloy exhibits a 6% increase in the ultimate tensile strength (UTS) and 130% increase in elongation. The enhanced strength and ductility could be attributed to the strengthening of the grain boundaries (GBs) by the unique microstructure design and the strain gradient associated with the structural gradient in heterostructures effectively eliminates the strain localization. Such a three-step heat treatment can be readily implemented in industrial practice for large-scale production and is applicable to a variety of precipitation-strengthened bulk alloys.

2. Method

2.1. Simulation method

We simulate the microstructure evolution of the Ti-55531 alloy during the two-step heat treatment process with the phase field method. The initial microstructure of the alloy is a duplex microstructure

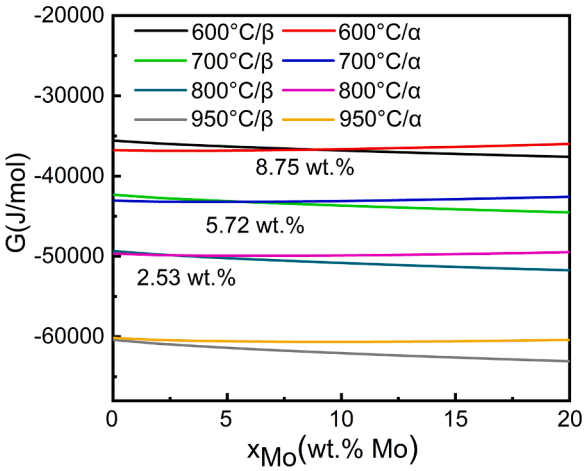

Fig. 1. The chemical-free energy curves of α and β phases for Ti-Mo binary alloys at various temperatures and the corresponding C_0 compositions.

contains globular α_p phase and β matrix, which are easily obtained in experiments by conventional thermal processing and heat treatment. In step 1, the alloy is up-quenched to β region (920 °C) for 300s, 500s, and 1000s, respectively, to dissolve structurally the globular α_p phase, but the holding times are too short to allow the solutes to homogenize, leaving composition modulations of different amplitudes in the β matrix. In step 2, the compositionally modulated alloys are isothermally aged at 600 °C for 1000s to obtain different heterostructures.

In our phase field model, the Ti-55531 alloy used in our experimental study was described using a pseudo-binary Ti-Mo system due to the lack of reliable thermodynamic and kinetic databases for the Ti-Al-V-Mo-Cr-Zr-Fe system. Specifically, we utilized the molybdenum equivalency (Mo-eq) (Eq. (1)) to represent the alloy, which preserves the phase stability of the alloy [22]. Therefore, the phase-field simulations presented in our manuscript serve only as a proof-of-concept guide for the experiment, as they capture the transformation kinetics of solute redistribution via long-range diffusion relative to the structural transformation by short-range diffusion. According to the following formula, Ti-55531 alloy can be simplified to Ti-9Mo (in weight percent).

$$\begin{aligned} MoE = {} & 1.0(wt.\%Mo) + 0.67(wt.\%V) + 0.44(wt.\%W) + 0.28(wt.\%Nb) \\ & +0.22(wt.\%Ta) + 2.9(wt.\%Fe) + 1.6(wt.\%Cr) + 1.25(wt.\%Ni) \\ & +1.70(wt.\%Mn) + 1.70(wt.\%Co) - 1.0(wt.\%Al) \end{aligned} \tag{1}$$

The chemical-free energy curves of the β and α phases in this pseudo-binary system at different temperatures obtained from the PANDAT thermodynamic database are shown in Fig. 1. A conserved order parameter, i.e., the concentration field (c), and 3 non-conserved structure order parameter fields, η_p ($p = 1\sim3$) are introduced in the phase field model to characterize the α+β microstructure in two-dimensions (2D). The total free energy of the system is formulated as a functional of the concentration and structural order parameter field as the following [23]:

$$\begin{aligned} F = {} & \int_V \left[\sum_p h(\eta_P) g_\alpha(c_{Mo}, T) + \left(1 - \sum_P h(\eta_P)\right) g_\beta(c_{Mo}, T) \right. \\ & \left. + \omega_1 \sum_{p \neq q} \eta_P \eta_q + \omega_2 \left(\eta_P^2 - 2\eta_P^3 + \eta_P^4\right) + \frac{k}{2} (\nabla c_{Mo})^2 + \frac{\varepsilon}{2} \sum_P (\nabla \eta_P)^2 + E^{dislocation} \eta_P^2 \right] + E^{elastic}(T) \end{aligned} \tag{2}$$

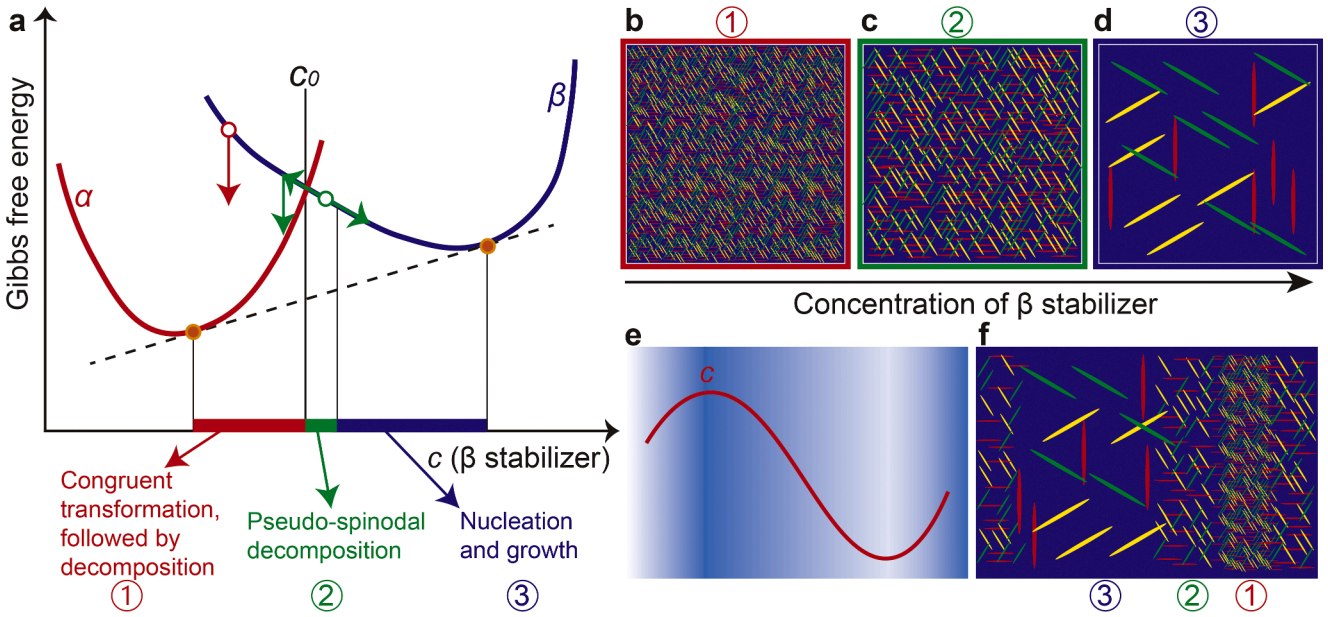

Fig. 2. Schematic diagram of variation of α phase precipitation mechanisms as a function of alloy composition. (a) Schematic diagram of the free energy curves of the α and β phases as a function of β stabilizer concentration. When the alloy composition is located to the left of the critical point (C_0) (the red concentration region), congruent β→α structural transformation (the red arrow) takes place, followed by solute partitioning, leading to an ultra-fine α precipitate microstructure (b). When the alloy composition is located on the right of the C_0 point and close to it (i.e., the green composition range), thermal fluctuations will bring some local compositions across the C_0 point (see one of the green arrows), and the precipitation follows the so-called pseudo-spinodal decomposition mechanism, leading to a fine α precipitate microstructure (c). When the alloy composition is on the right side of the C_0 point and far away from it (e.g., the blue composition range), α precipitation will follow the classical nucleation-and-growth mechanism, leading to a relatively coarse α precipitate microstructure (d). (e–f) When a composition modulation is present in the β matrix (e), different precipitation mechanisms will operate simultaneously, resulting in a gradient precipitate microstructure (f).

where, the η_p represents structural order parameter of the p_{th} α variants (similarly, η_q represents the q_{th} α variant), and c_{Mo} denotes the concentration of *Mo*. h(η_i) is an interpolation function which links a smooth connection of the free energy curves between structural order parameters and concentration [24].

$$h(\eta) = \eta^3\left(6\eta^2 - 15\eta + 10\right) \tag{3}$$

w_1 and w_2 are the surface hump height among different α variants and between β and α phases, respectively. κ and ε characterize the gradient energy coefficients for concentration and structural field, respectively [9]. The chemical free energy expressions for the α and β phase as functions of composition and temperature, denoted as $g_\alpha(c_{Mo},T)$ and $g_\beta(c_{Mo},T)$ respectively, have been derived based on the free energy curves depicted in Fig. 1. The C_0 compositions are 8.75 wt.% Mo, 5.72 wt.% Mo and 2.53 wt.% Mo at temperatures of 600 °C, 700 °C and 800 °C, respectively. it is important to note that there is no C_0 point identified at 950 °C.

The contribution of elastic energy to the total free energy is closely to temperature. If the temperature above 800 °C, the elastic energy is negligible due to the assumption of the uncoherent boundary [25]. If the temperature below 800 °C, the coherent boundary is assumed in our simulations, and the elastic energy as a nonnegligible term in solid state phase transition can be derived according to Khachaturyan-Shatalov theory as follows:

$$E^{elastic} = \frac{1}{2}\int_V \frac{d\vec{k}}{2\pi^3}\sum_{p,q}^{3} B_{pq}(\vec{n})\tilde{\eta}_P\left(\vec{k}\right)\tilde{\eta}_q^*\left(\vec{k}\right) \tag{4}$$

$$B_{pq}(\vec{n}) = C_{ijkl}\varepsilon_{kl}^T(p)\varepsilon_{kl}^T(q) - \vec{n}\sigma_{ij}^T(p)\Omega_{ij}(\vec{n})\sigma_{kl}^T(q)\vec{n}_l \tag{5}$$

Where $C_{ijkl}$is the stiffness tensor, $\varepsilon_{ij}^T(p)$ is the stress-free transformation strain of the p_{th} variant, and $\sigma_{ij}^T(p) = C_{ijkl}\varepsilon_{kl}^T$, $[\Omega(\vec{n})]_{ik}^{-1} = C_{ijkl}n_jn_l[\Omega(\vec{n})]$. The value of stress-free transformation strain for the three equivalent variants in 2D simulations on the $(11\bar{1})$ plane can be derived from the lattice constants [26], burgers orientation relationship [27] and symmetry operations.

$$\varepsilon_1 = \begin{pmatrix} 3.13998E-2 & 0 & 0 \\ 0 & -4.74681E-2 & 9.16523E-2 \\ 0 & 9.16523E-2 & 0 \end{pmatrix}$$

$$\varepsilon_2 = \begin{pmatrix} -2.77511E-2 & -3.41509E-2 & -7.93732E-2 \\ -3.41509E-2 & 1.16830E-3 & -4.58262E-2 \\ -7.93732E-2 & -4.58262E-2 & 0 \end{pmatrix}$$

$$\varepsilon_3 = \begin{pmatrix} -2.77511E-2 & 3.41509E-2 & 7.93732E-2 \\ 3.41509E-2 & 1.16830E-3 & -4.58262E-2 \\ 7.93732E-2 & -4.58262E-2 & 0 \end{pmatrix}$$

The microstructural evolution of structure and concentration diffusion can be obtained by solving two partial differential equations: Allen-Chan (AC) and Chan-Hilliard (CH) for structure field and concentration field respectively.

$$\frac{\partial c_{Mo}}{\partial t} = \nabla\left(M\nabla\frac{\delta F}{\delta c_{Mo}}\right) + \xi_c \tag{6}$$

$$\frac{\partial \eta_p}{\partial t} = -L\frac{\delta F}{\delta \eta_p} + \xi_\eta \tag{7}$$

Where L stands for the structural mobility(η_P) and M stands for the chemical mobility (c_{Mo}). ξ_c and ξ_η are the Langevin force terms used to simulate thermal fluctuation [28].

2.2. Experimental method

A commercially available Ti-55531 alloy is used in this study. The chemical composition of the alloy is 5.2Al, 5.3 V, 5.1Mo, 2.8Cr, 1.1Zr, 0.3Fe, 0.02C, 0.002H, 0.11O, 0.003 N and 0.08Si,all weight percent. The

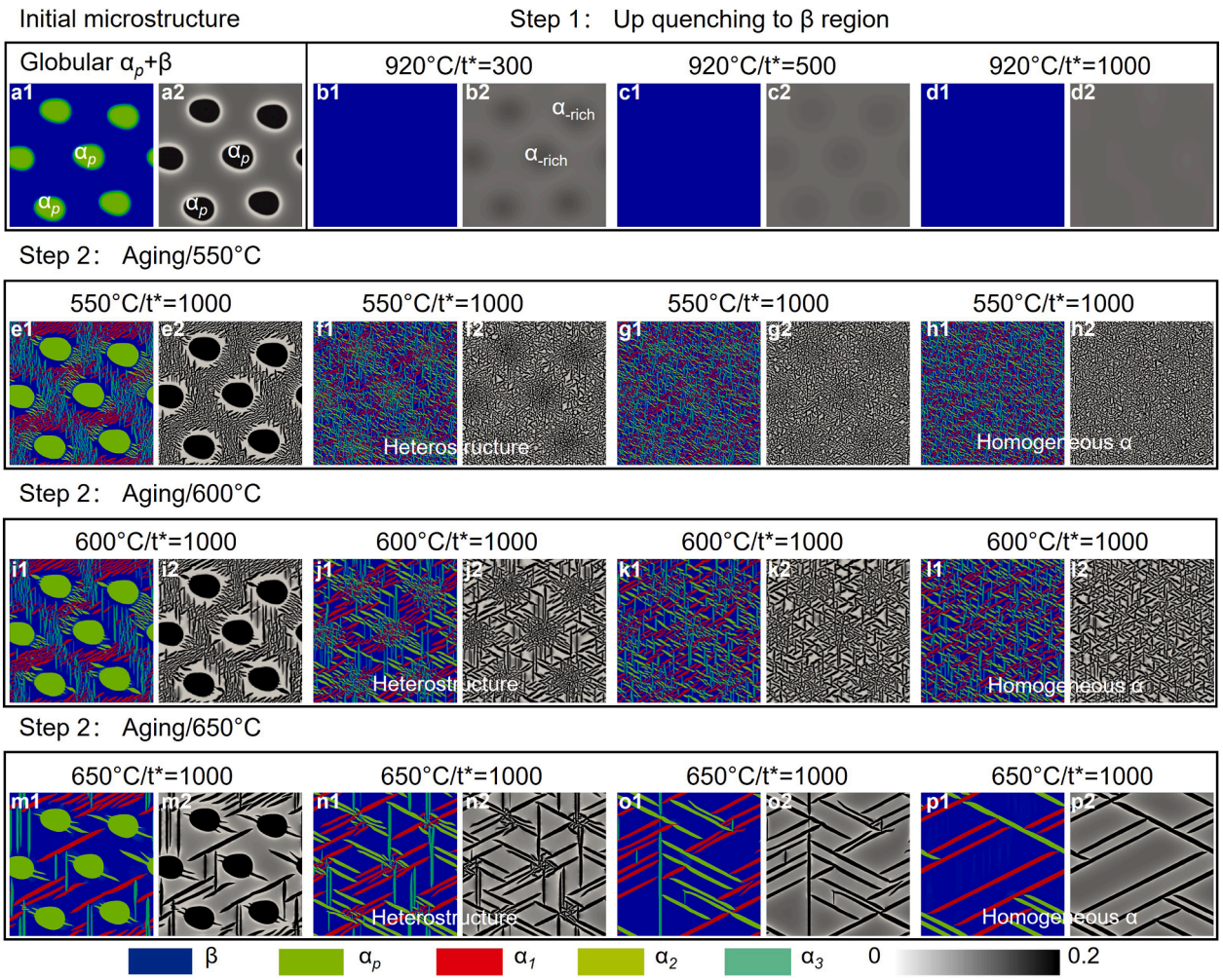

Fig. 3. Calculated α precipitate morphology designed by two-step heat treatment. (a) The initial microstructure of Ti-9Mo binary alloy contains globular α_p phase and β matrix. In Step 1: (b-d) the alloy is up-quenched to β phase region (920 °C) for t*=300s (b), t*=500s (c) and t*=1000s (d), respectively. The α_p phase is dissolved but the concentration distribution is retained, and the solute elements gradually diffuse evenly with the increase of the solution time. In Step 2: (e-p) the binary systems are aged at 550, 600 and 650 °C for t*=1000s, (e, i, m) bimodal microstructure contains globular α_p and lamellar α phase, (f, j, n) heterostructure contains significantly different coarse and ultra-fine α plates, (g, k, o) heterostructure contains coarse and fine α plates, (h, l, p) homogeneous α plates. The color figures describe the structural field (red, green and blue colors represent three variants of the α precipitates, and the dark blue color describes the β phase). The black-gray figures describe the concentration field (black represents α precipitates, gray represents β phase, and dark gray represents residual concentration in β phase).

β-transus temperature is 830±5 °C using the metallographic method. According to the simulation results, a three-step heat treatment is designed for the alloy to obtain heterostructure, as shown in Supplementary Fig. 1. Since the α_p phase in the as-received forged alloy has not yet been globularized, an additional heat treatment step is required to globularize the α_p phase. Step 1: the alloy is annealed in the α+β two-phase region (800 °C) for 90 min to obtain globular α_p + β matrix. Step 2: up-quenching to the single β phase region (920 °C) and isothermally hold for short time (3, 5 min) to transform structurally the globular α_p phase to β phase, but maintain the solute partition in the two phases. Because a complete homogenization of solute elements requires a solution time more than 30 min at 920 °C. In step 3: the compositionally modulated alloys are aged at 600 °C for 120 min to obtain the heterostructures and, as comparison, a fully homogenized alloy (solution treatment at 920 °C for 30 min in Step 2) is also aged at 600 °C for 120 min to obtain the homogeneous structure. In this study, the area fractions of the coarse and ultra-fine α phase regions are determined using the square-counting method. Subsequently, the thickness distribution of the lamellar α phase within these regions is calculated by measuring the length after scribing. The obtained thickness distributions are then multiplied by their corresponding area fractions to calculate the frequencies of different thicknesses. Furthermore, the phase fractions of the lamellar α and β phases are obtained using the dot-counting method. This method allows for the determination of the relative proportions of these phases within the microstructure.

The heat-treated alloys are processed into dog-bone like samples, and tensile tests are carried out at the room temperature. The size of the uniform part of the tensile sample is 20 mm × 3.5 mm × 1.5 mm, and the stretching rate is 1 mm/min. Tensile tests were performed on MTS 810 system, and each set of specimens was tested at least three times. SEM is used to characterize the microstructures of heterostructured and homogeneous alloys before and after the tensile fracture. TEM is used to characterize the deformation microstructure. The TEM samples were first polished to 60 μm with SiC sandpaper, and then thinned in TENUPOL-5 electrolytic thinning instrument with a voltage of 25 V and a temperature of minus 25 °C. The TEM characterization of this study is performed on Titan G2 60–300 with a working voltage of 300 KV. The SEM characterization is performed on TESCAN MIRA3 LMH with an acceleration voltage of 15 KV and a working distance of 15 mm. The composition of the phantom α_p and β phase is measured on a JEOL JXA-8230 electron probe micro-analysis (EPMA) with parameters of 15 kV and 20 nA.

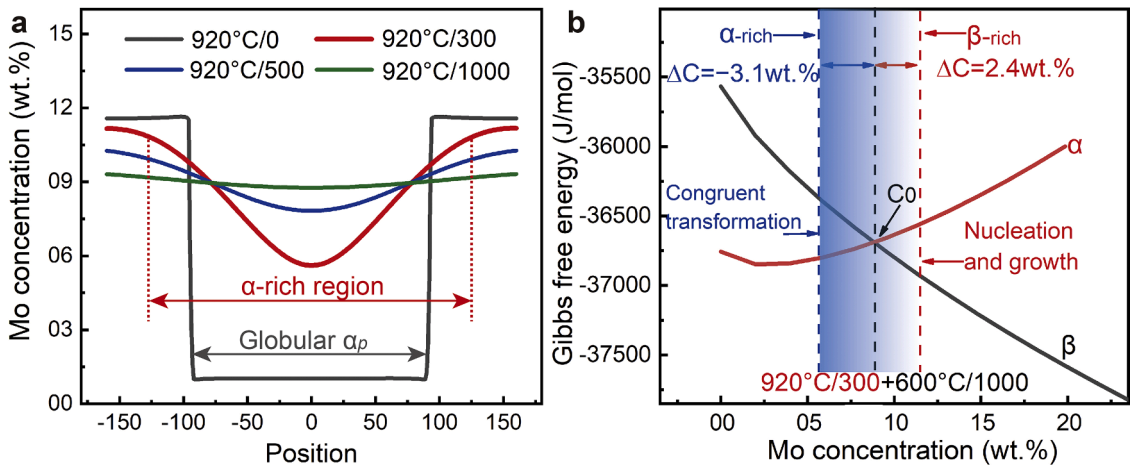

Fig. 4. The formation mechanism of heterostructures. (a) The concentration profiles across a phantom α_p in the Ti-9Mo alloy after being up-quenching to β-phase region (920 °C) for t* = 0, 300, 500 and 1000s. As the solution time increases, the α_p phase is dissolved and left the concentration hysteresis area (phantom α_p), the β phase concentration gradually changes from heterogeneous to homogeneous. Compared with α_p, the area of ghost α_p doubles (t*=300s) or even more (t*=500s). (b) The free energy curves of α and β phases at 600 °C, and the relationship between C_0 and β-rich and α-rich concentrations after treated at 920 °C for t*=300s. Due to the Mo concentration varied continuously from 5.6 to 11.2 wt%, all three precipitation mechanisms shown in Fig. 2 are activated. In the α-rich region, the α phase transition is congruent structural transformation followed by decomposition, and in the β-rich region is the nucleation and growth mechanism.

3. Results and discussion

3.1. Variation of precipitation mechanisms with composition in α+β Ti alloys

The designed heat treatment schedule to prepare the heterostructured titanium alloys is based on multiple precipitation mechanisms, which vary with alloy composition. As illustrated in Fig. 2a, when the alloy composition is located on the left side of a critical point (C_0), a congruent β→α structural transformation takes place. The critical point C_0 represents the composition where the α and β phase free energy curves intersect (within the red composition range in Fig. 2a). Because of the relatively large precipitation driving force and no need for solute partition, the congruent structural transformation creates ultra-fine α precipitates (Fig. 2b) [22,29]. When the alloy composition is located on the right side of the C_0 point and close to C_0 (e.g., the green composition range in Fig. 2a), thermal fluctuations will make certain local compositions across the C_0 point and activate the congruent β→α structural transformation, followed by solute partitioning, leading to fine α precipitates (Fig. 2c). This is the so-called pseudo-spinodal decomposition mechanism [26,30]. When the alloy composition is on the right side of the C_0 point and far away from it (e.g., the blue composition range in Fig. 2a), the β→α transformation follows the classical nucleation-and-growth mechanism, leading to a significantly coarser α precipitate microstructure (Fig. 2d) [23,26,31]. This variation of precipitation mechanisms with alloy composition offers us an opportunity to design heterostructure with well controlled precipitate microstructure gradients (Fig. 2f) by creating final scale concentration modulations in the parent β phase (Fig. 2e).

3.2. Phase field simulation of heterostructure formation

In order to activate the various precipitation mechanisms of the α phase in a single alloy, a two-step heat treatment process is designed and simulated for a prototype binary alloy, Ti-9Mo (in weight percent), representing Ti-55531 alloy (see Method for details) by the phase field method. Fig. 3a shows that the initial state of the alloy is a duplex microstructure contains globular α_p phase and β matrix, and the area fraction of globular α_p is about 20%. In Step 1, the sample is up-quenched to the single β phase region (920 °C) and isothermally hold for t*=300, 500 and 1000, respectively, where t* is a reduced time, and then rapidly quenched to room temperature. Based on the observations from Fig. 3b, 3c, 3d, it is evident that the globular α_p precipitates undergo a complete structural transformation from HCP to BCC during the specified holding times. However, the homogenization of Mo concentration within the precipitates requires an extended period of time (e.g., at t*=1000). For instance, at t*=300, the phantom globular α_p are still visibly present (Fig. 3b) and they gradually diminish with longer aging times (as seen in Fig. 3c and 3d). This leads to alternating α stabilizer rich and α stabilizer lean regions in the β matrix.

In Step 2, all the samples are quenched to and aged at 550~650 °C. This leads to various α+β microstructures, including bimodal microstructure composed of globular α_p and lamellar α phase (Fig. 3e, 3i, 3m), heterostructure with alternating coarse and ultra-fine α plates (Fig. 3f, 3j, 3n), coarse and fine α plates (Fig. 3g, 3k, 3o), and homogeneous α plates (Fig. 3h, 3l, 3p). At the same aging temperature, the size scale of the α plates in homogeneous structure is in between those of the ultra-fine and coarse α plates in heterostructure. With the increase of aging temperature, both coarse and ultra-fine α plates are coarsened in different magnitudes. When the aging temperature is 600 °C, the difference between the coarse and ultra-fine α plates is most significant (Fig. 3j). Note that the size of the coarse α plates in Fig. 3k are finer than those observed in Fig. 3j because of the difference in the amplitude of the Mo concentration modulations (as shown in Fig. 3b and 3c). Thus, the size difference between the ultra-fine and coarse α plates can be easily adjusted by controlling the solution time and aging temperature.

In order to understand the formation mechanism of heterostructure with ultra-fine and coarse α plates, we calculate the concentration of Mo (a strong β stabilizer) across a phantom α_p of the duplex microstructure after up-quench to the single β phase region (920 °C) and isothermal hold for different times (t*=0, 300, 500 and 1000s) (Fig. 4a). At t*=0, the initial concentrations of globular α_p and β phases are 1 wt.% and 11.5 wt.% Mo, respectively, with a difference of 10.5 wt.% Mo (the gray curve). At t*=300s (the red curve), the Mo-lean region expanded to approximately twice the area (measured in square units) of the original globular α_p, while the Mo concentration varied between 5.6 wt% and 11.2 wt% from the center to the edge. At t*= 500s (the blue curve), the size of the Mo-lean region further increased to about three times of its original size with the Mo concentration ranging from 7.8 wt.% and 10.2 wt.%. As t*=1000s (the green curve), the Mo concentration approaches to uniform. The free energy curves of α and β phases of Ti-Mo system at 600 °C are shown in Fig. 4b, where the C_0 point is located at 8.75 wt.%

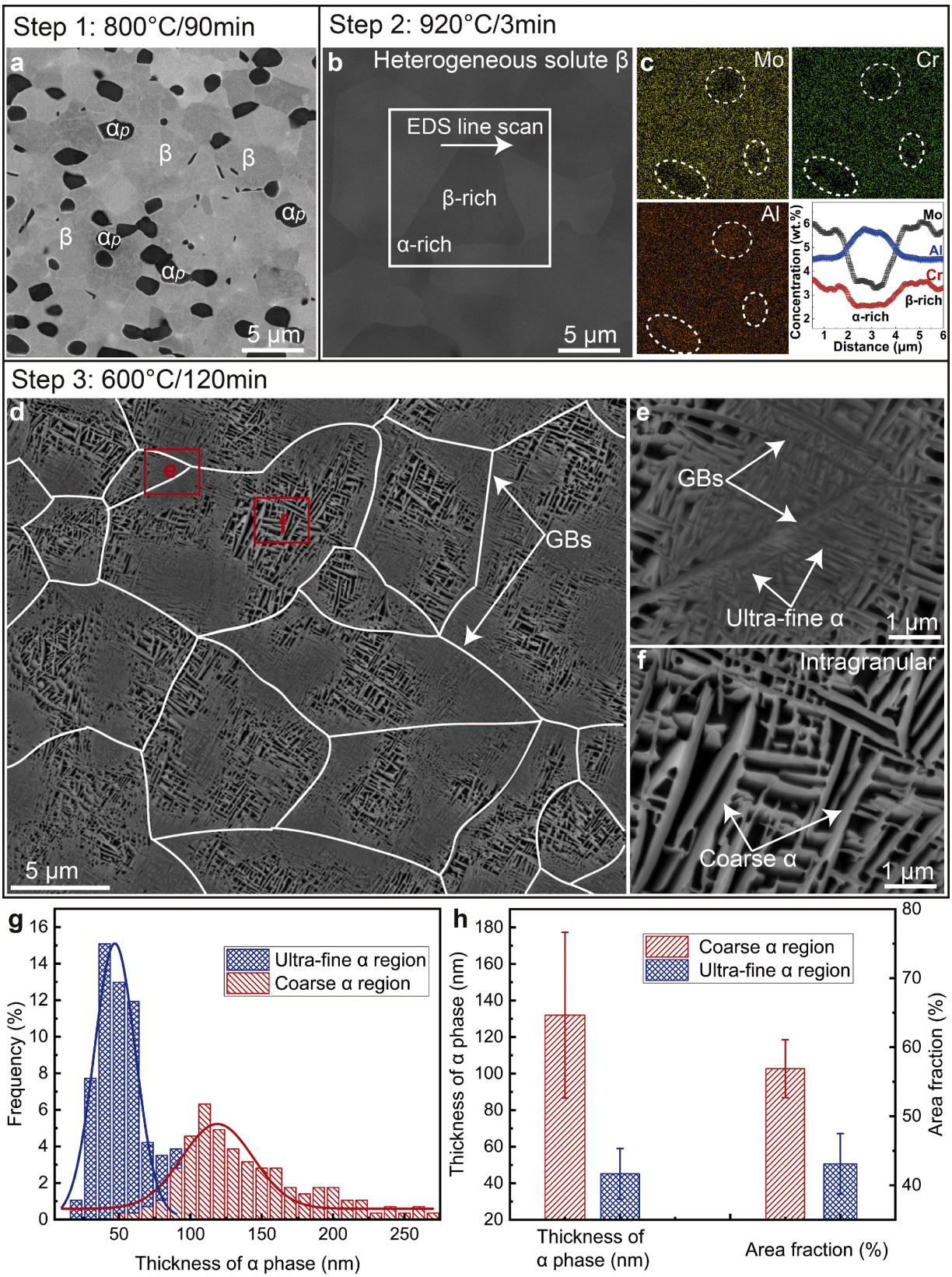

Fig. 5. Ti-55531 alloy obtains the heterostructure through three-step heat treatment. In Step 1: (a) the alloy is annealed in the α+β region (800 °C) for 90 min to globularize the α phase, and a duplex microstructure contains globular α_p and β matrix are obtained. In Step 2: (b-c) up-quenching to β region (920 °C/3 min) and then air-cool, the globular α_p phase is dissolved, and leaves the α stabilizer rich pockets (at the β GBs). (c) the concentration distribution of element Mo, Cr, Al, and the concentration profile along the white arrow in Fig. 5b, including the α-rich and β-rich regions. In Step 3: (d) the alloy is aged at 600 °C for 120 min to obtain the heterostructure, and (e) the ultra-fine α phase covers most of the GBs, (f) coarse α phase within the grain. (g) Distribution characteristics of α-lamellar thickness in the heterostructure, (h) Average thickness of coarse and ultra-fine α lamellae, and area fractions of coarse and ultra-fine α precipitate regions.

Table 1
EPMA determined phantom α_p and β phase compositions and the corresponding Mo equivalencies.

Phase	Compositions (wt.%)						
	Mo	V	Cr	Al	Fe	Zr	Cumulative Mo-eq
Phantom α_p	3.3	4.7	2.4	5.6	0.16	1.1	5.4
β phase	5.5	5.6	2.9	4.8	0.34	1.0	10.6
Mo-eq difference	2.2	0.74	0.9	0.8	0.5	0.03	5.2

Mo that is right in the middle of the concentration modulation across the phantom α_p that has been up-quenched and held for t*=300s (5.6wt% to 11.2wt% Mo). When the alloy is aged at 600 °C, all three precipitation mechanisms shown in Fig. 2 are activated, leading to the heterostructure shown in Fig. 3j. When the dissolution time is t*=1000s, the nearly homogeneous Mo concentration is close to the intersection point (C_0) of the free energy curve (ΔC = 9 wt.%−8.75 wt.% = 0.25 wt.% << 2 wt. %). Therefore, α precipitation follows the pseudo-spinodal decomposition mechanism, leading to homogeneous and fine α precipitates (i.e., homogeneous structure) (Fig. 3l). This is consistent with the results of Nag et al. [9]. In heterostructure, the ultra-fine α phase formed in the α stabilizer rich region is via congruent structural transformation followed by decomposition, while the coarse α phase formed in the α stabilizer lean region is via the nucleation-and-growth mechanism.

It should be noted that in the phantom α_p regions, the concentration of β-stabilizer is lower than that of the β matrix of the homogeneous alloy and, thus, the α phase has greater driving forces for precipitation in these regions. In contrast, the β stabilizer concentration in the β matrix of the heterostructure samples is higher than that of the homogeneous alloy and, thus, the driving force for α precipitation is smaller. This would also lead to alternating finer and coarser α precipitate microstructures as compared to that observed in the homogeneous alloy. Thus, the variation of β matrix composition associated with the phantom α_p causes the variation of β phase stability and α precipitation mechanisms, which are responsible for the formation of the heterogeneous precipitation microstructure.

3.3. Three-step heat treatment to prepare heterostructured alloy

According to the simulation results, we design a three-step heat treatment for Ti-55531 alloy to obtain heterostructure. Since the α_p phase in the as-received forged alloy has not yet been globularized, we need to add one more step, i.e., the globularization treatment. In Step 1, the as-received alloy is annealed at 800 °C (α+β phase region) for 90 min (Fig. 5a) to obtain the duplex microstructure with globular α_p phase and β matrix. If the starting alloy has already a duplex microstructure, then this step can be skipped. The globular α_p are mostly located at triple junctions of the β GBs. The diameter of the globular α_p is about 1∼3 μm and its area fraction is about 20%.

In Step 2, the alloy is up-quenched (∼1000 °C/min) to β phase region (920 °C) and held for 3 min (Fig. 5b-c). SEM (Fig. 5b) and TEM (Supplementary Fig. 2) results show that the globular α_p have been dissolved and the alloy has a single phase β. The concentration mapping results in Fig. 5c show that the alloying elements are heterogeneous in the β phase. The metastable island regions lean in β stabilizers (Mo, V, Cr) and rich in α stabilizers (Al) are centered at the original globular α_p locations and spread into the surroundings.

Table 1 presents the compositions of α_p and β matrix regions, as determined by EPMA, along with the difference in their corresponding Mo equivalencies. The Mo equivalencies are obtained using Eq. (1). The results demonstrate a concentration variation of approximately 5.2 Mo equivalency, which is consistent with the calculated results of 5.6 Mo equivalency. Additionally, the regions located between these phantom α_p regions, predominantly situated in the interior regions of the β grains, exhibit higher contents of β stabilizers and lower contents of α stabilizers. Consequently, there is a gradual decrease in the concentration of α stabilizers and a corresponding increase in the concentration of β stabilizers from the GBs towards the grains interiors.

During Step 3, the alloy is aged at 600 °C for 120 min (Fig. 5d-f), which leads to the formation of a heterostructure comprising an alternating distribution of coarse and ultra-fine α precipitates. This can be attributed to the presence of a heterogeneous β matrix with large number of fine domains that are alternately enriched or depleted in α stabilizers, as obtained in Step 2. Based on the results in Table 1, the Mo equivalence of the heterogeneous β matrix ranges from 5.4 to 10.6. This variation enables the activation of all three precipitation mechanisms, aligning with the findings of the phase field simulations. It is important to note that a large number of the β GBs are covered by the ultra-fine α precipitates (Fig. 5e), while the coarse α precipitates are predominantly distributed within the interiors of the grains (Fig. 5f). This distribution pattern arises because the ultra-fine α precipitates are formed in the phantom α_p regions, which primarily occur at triple junctions of β GBs (where the globular α_p precipitates are located). Moreover, during dissolution, the area fraction of the phantom α_p regions expands by 2 to 3 times, resulting in a significant coverage of the GBs. Fig. 5g quantifies the thickness distribution of the α precipitates in the heterostructures, which exhibits a significant bimodal characteristic. In the coarse α phase region, the average thickness of the α lamellae is ∼132±45 nm, while in the ultra-fine region it is 45±13 nm. The area fractions occupied by the coarse and ultra-fine α regions are ∼56.9% and 43.1%, respectively (Fig. 5h).

As a comparison, the homogeneous structure (Fig. 6) is obtained by prolonged the homogenization solution treatment time of Step 2. In Step 1 (Fig. 6a), the alloy is treated at 800 °C for 90 min (consistent with Fig. 5a). In Step 2, the alloy is up-quenched to 920 °C for 30 min. SEM images (Fig. 6b) show that the alloy is a single β phase. Fig. 6c shows the results of concentration mapping. After 30 min homogenization annealing in β phase region, the alloying elements are fully diffused evenly, and there is no concentration difference between at GBs and within grain. In Step 3, aging the alloy at 600 °C for 120 min (Fig. 6d-f), homogeneous and fine lamellae α are precipitated in the homogeneous metastable β matrix. The enlarged images (Fig. 6e-f) show that there is no significant difference in the size of the α phase near the GBs and within the grain. Fig. 6e shows a continuous layer of coarse α phase at GBs. Fig. 6g-h quantifies the α lamellar thickness distribution of the homogeneous structure. The average thicknesses of the α lamellae is ∼79 ± 21 nm, respectively, and the area fraction of the α phase is ∼53.7%.

3.4. Tensile properties of heterostructured alloy

Our approach to designing heterostructured alloy results in a notably improved strength and ductility. This is revealed by comparing the heterostructured alloy with a reference alloy with the homogeneous structure (Fig. 7). When the aging temperature is 600 °C, the UTS of the homogeneous structure (see Fig. 6) reaches 1210 MPa and the total elongation is 4.3%, while the UTS of the heterostructure (see Fig. 5) reached 1286 MPa, increased by 76 MPa (6%) and, more significantly, the uniform elongation of the alloy reached 10.1%, increased by 130%. When the aging temperature is 500 °C, the heterostructured alloy achieves an ultra-high strength of 1496 MPa while maintains a 5.8% uniform elongation. Fig. 7b compares the tensile properties of our heterostructured alloy with Ti-5553, Ti-1023 and other titanium alloys with homogeneous or heterogeneous structure [32–38]. It can be seen

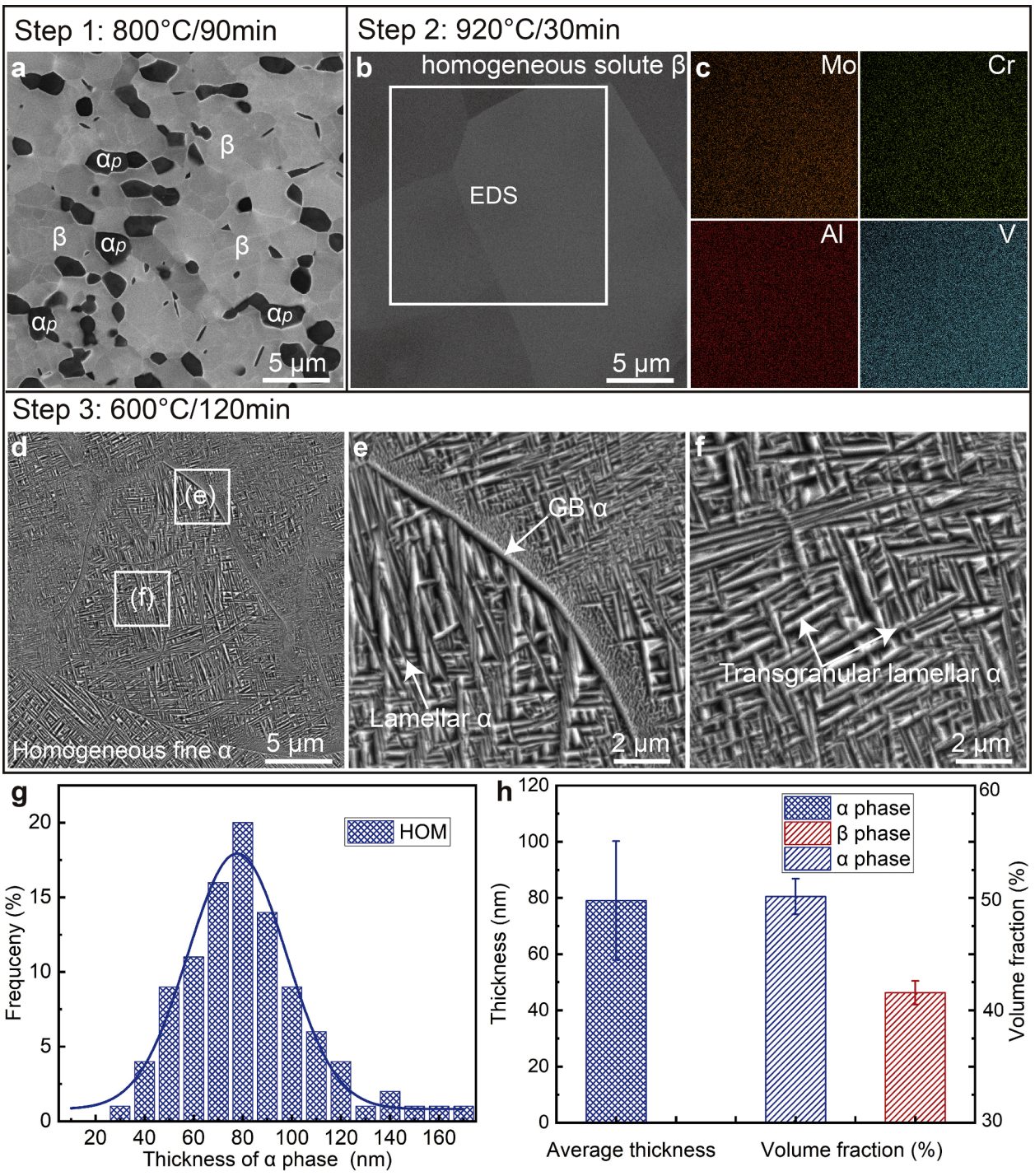

Fig. 6. Compared with Fig. 5, homogeneous structure is obtained by prolonged homogenization solution treatment time. In Step 1: (a) consistent with Step 1 in Fig. 5a, the alloy is treated at 800 °C for 90 min and then air-cooled to obtain α_p and β matrix. In Step 2: (b-c) the alloy is up-quenched to 920 °C/30 min and then air-cool, the α_p phase is dissolved and diffused uniformly, (c) the homogeneous concentration distribution of element Mo, Cr, V, Al. In Step 3: (d-f), (d) the alloy is aged at 600 °C for 120 min to obtain the homogeneous structure, (e-f) uniformly dispersed α phases near the GBs and within the grains, and coarse α phase along the GB. (g) Normal distribution of α-lamellar thickness in the homogeneous structure. (h) Average thickness of the α phase, area fraction of the α and β phases.

that the heterostructure has excellent mechanical properties and achieves a synergy between strength and ductility.

3.5. *Deformation and fracture mechanism of heterostructured alloy*

To compare the deformation and fracture mechanisms between the heterogeneous and homogeneous alloys, post-failure specimens are examined, as illustrated in Fig. 8-9 and Supplementary Fig. 3. These examinations provide insights into the differences in how the alloys deform and fracture under different conditions. In the homogeneous alloy, since the strength of the GB α phase (α phase precipitated along the GBs, see Fig. 6e) is lower than that of the intragranular lamellar α regions, deformation initiates within the GB α phase regions, resulting in a low yield strength [39,40]. Afterwards, strain localization at the GBs causes microcracks to nucleate and propagate along the GBs [19,41,42] (Fig. 9a-d). Due to the premature intergranular brittle fracture, the stress

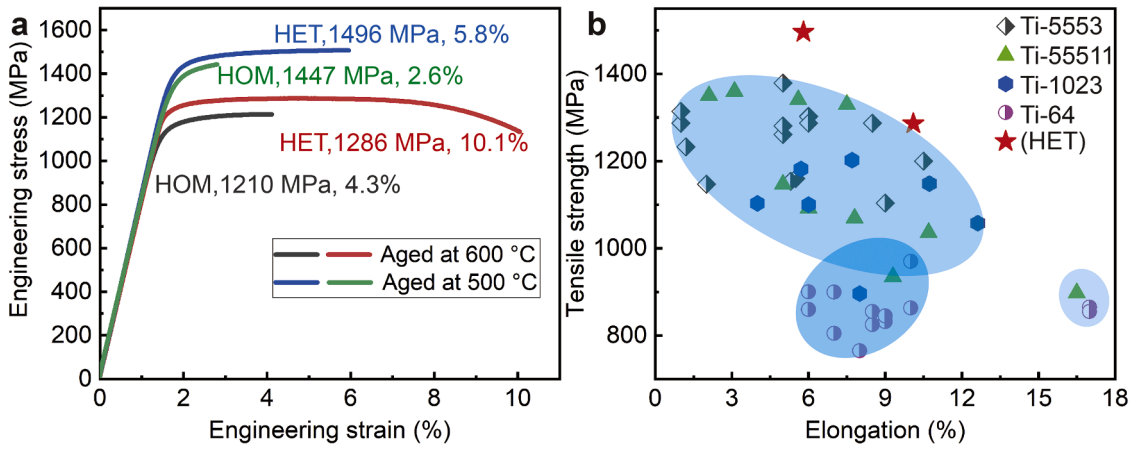

Fig. 7. Comparison of tensile properties between heterostructure and homogeneous structures. (a) The heat treatment system of heterostructured alloy is 800 °C/90 min + 920 °C/3 min + 500/600 °C/120 min, and homogeneous alloy is 800 °C/90 min + 920 °C/30 min + 500/600 °C/120 min. (b) Comparison of tensile properties between heterostructured alloy in this study and other alloys [32–38].

level is not high enough to activate the deformation in the intragranular lamellar α phase regions and, thus, only low density of dislocations are detected in the intragranular α phase regions (Supplementary Fig. 3).

The enhanced ductility of the heterostructure could be attributed to its unique microstructure that avoids strain localization, allowing continued deformation by dislocations and twinning in the coarse and ultra-fine α precipitate regions. First, since the globular α_p are usually located at triple junctions of β GBs, and after becoming phantom α_p they double their area or even more, the ultra-fine α phase regions in heterostructure formed within these phantom α_p cover most of the GBs (Fig. 5d). The GBs covered by the ultra-fine α phase are significantly strengthened, and thus avoid strain localization and early microcracks nucleation there, result in an increase in yield strength. For example, Fig. 9f shows that the nucleation sites of microcracks are at intragranular coarse α phase regions rather than GBs, which lead to tortuous transgranular ductile fractures (Fig. 9e-h). Because of the reduced strain localization at the GBs, the intragranular coarse α phase in heterostructure enables large-scale deformation through the accumulation of high density of dislocations (Fig. 8b and Supplementary Fig. 4) and deformation twinning (Fig. 8c-e), which will significantly increase ductility of the alloy [43–46].

Second, as the soft coarse α region is surrounded by the hard ultra-fine α region, dislocations are stacked at the interface between the soft and hard regions (Fig. 8a), forming geometrically necessary dislocations to coordinate the deformation of the soft and hard regions. Fig. 8a and 8g-h demonstrate the high density of dislocations and nanotwins in the interface region, which further increases the ductility of the alloy.

In addition, the high density of dislocations in the coarse α region and the geometrically necessary dislocations at the interface form a strain gradient that further prevents strain localization and stimulates deformation in the ultra-fine α region. Fig. 8a and 8j-l show the gradually decreasing dislocation density gradient (strain gradient) from the coarse to ultra-fine α regions, and the dislocation and twin deformation in the ultra-fine α regions, respectively. According to the back stress theory [4,47,48], the strain gradient formed between the soft and hard regions will create a long-range back stress within the soft regions, which will significantly strengthen the soft regions and eventually activate plastic deformation of the hard region (ultra-fine α phase region) (Fig. 8j-l), leading to further increase in ductility [44,46,49,50].

Interestingly, twinning deformation are detected in the coarse, ultra-fine and interface regions in the heterostructures. According to previous reports [51,52], twinning preferentially occurs in coarse lamellae (thickness over 200 nm) or globular α_p particles. However, the thickness of the ultra-fine α lamellae in the heterostructures is only ~50 nm (Fig. 8j). Nanotwins in such ultra-fine α are rare in titanium alloys [53, 54]. According to Guo et al. [55] the formation of twins in titanium alloys is related to the stacking fault energy and local stress state. Fitzner et al. [56] reported that an increase in Al content decreases the stacking fault energy on the twinning plane, which will enhance the twinning activity. However, the Al contents in the coarse and ultra-fine α precipitates measured by EDS are 7.5 and 7.1 wt.%, respectively, while the one in the homogeneous structure is 7.3 wt% [22]. We thus attribute the formation of nanotwins in the heterostructures to high local stresses. It has been shown that the stress state plays a decisive role in twin formation [56]. In the heterostructures, twin formation is usually accompanied by dislocations pile-up at the α/β interface (Fig. 8c, 8g, 8j), which suggests that twin formation is associated with the high local stresses. The unique heterostructures in this study effectively avoids strain localization and allows the material be loaded to a higher stress level and, thus, promotes the formation of nanotwins.

3.6. Strengthening mechanism of the heterostructured alloy

The high strength of the heterostructures could be attributed to the back stress effect caused by strain partitioning. Under tensile loading, the coarse α precipitate regions (soft regions) deform preferentially, but the deformation is confined by the surrounding hard regions (ultra-fine α precipitate regions). Dislocations are accumulated at the interfaces between the soft and hard regions (Fig. 8a, 8g-i), which generate long-range internal stresses in the soft regions, i.e., back stresses, in the direction opposite to the resolved shear stress direction. Therefore, further yielding of the soft regions requires overcoming this back stress, which strengthens the soft regions, somewhat similar to work hardening of the soft regions [57]. That is why the coarse α phase in the heterostructures is coarser than that in the homogeneous structure, but it has a greater yield strength than that in the homogeneous structure.

To investigate the influence of back stress on the yield strength, cyclic loading-unloading experiments on both homogeneous and heterogeneous alloys are conducted as shown in Fig. 10. The back stress σ_b is half of the unloading yield stress (σ_u) and reloading yield stress (σ_r), where the yield points (σ_u and σ_r) are determined by deviation of the stress strain curve from the effective Young's modulus [58]. The effective Young's modulus is the slope of the linear segment of the unloading and reloading curves, and here it is assumed that the unloading effective Young's modulus (E_u) and reloading effective Young's modulus (E_r) are equal. As shown in Fig. 10b, the calculated back stress for the heterostructure during early deformation is approximately 640 MPa, while that for the homogeneous alloy is 585 MPa. This indicates that the soft zone in the heterostructure needs to overcome higher back stress to initiate plastic deformation. The elevated back stress in the

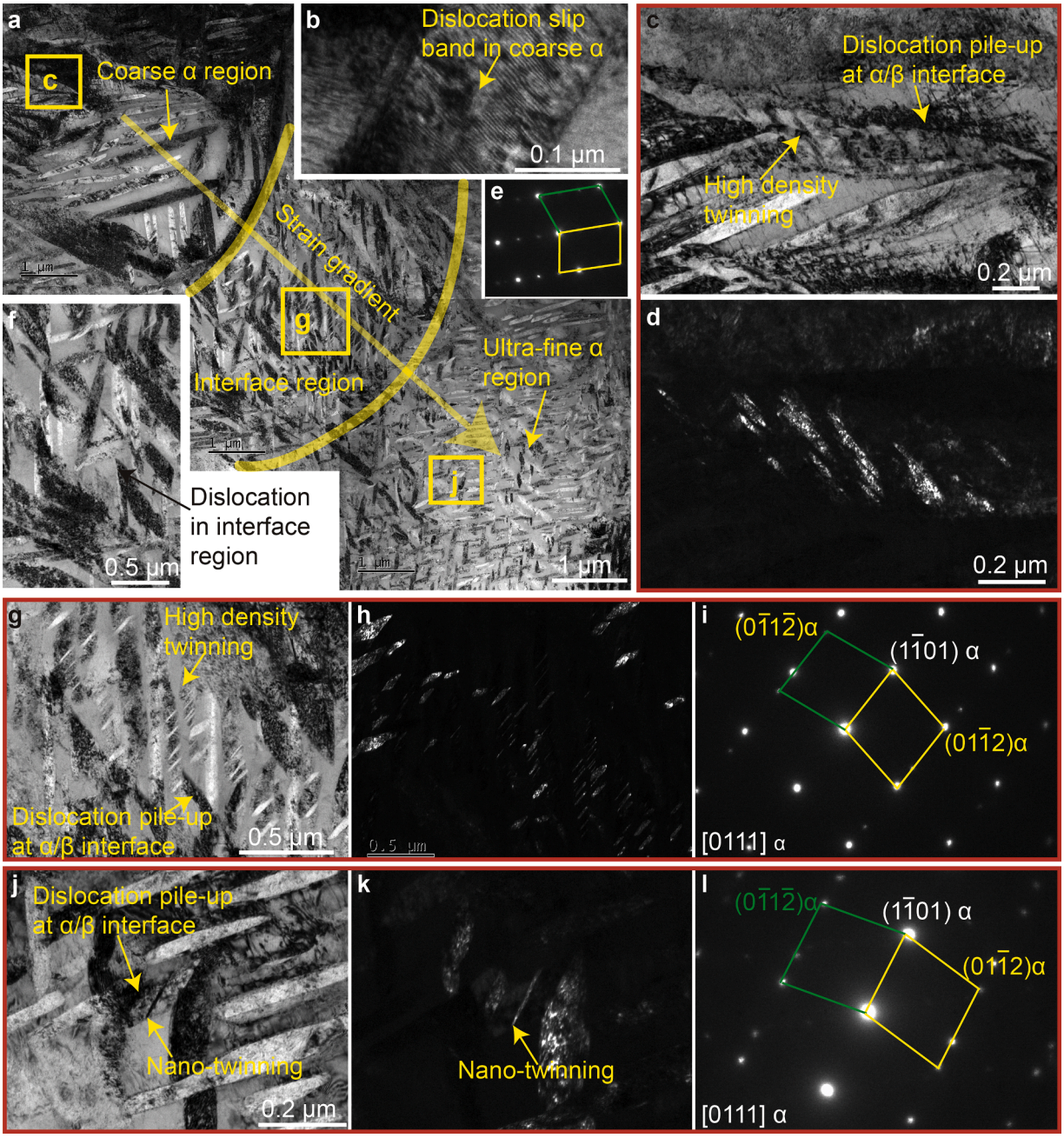

Fig. 8. Deformation mechanism of heterostructures (the same specimen as Fig. 5d). (a) Dislocation density and strain gradients formed between coarse, ultra-fine and interface regions. (b) High-density dislocations slip band in the coarse α phase. (c-e) Deformed twins in coarse α region (c) Dislocation accumulation at the α/β interface induces twinning deformation. (d) Bright field images of the twin system, (e) selected area electron diffraction of deformed twins in coarse α. (f) High-density dislocations in the interface regions. (g-i) High-density deformation twins in the interface regions, (g) bright field image, (h) dark field image, (i) diffraction spots showing {1$\bar{1}$01} twins. (j-l) Nanotwins in ultra-fine α precipitates. (j) Dislocation pile-up at the α/β interface, inducing nanotwins. (k) dark field image, (l) selected area electron diffraction.

heterostructure can be attributed to its significant strain partitioning effect, as evidenced by the strain gradient in Fig. 8a and the pronounced strain hysteresis loop in Fig. 10b [59]. Previous research has indicated that a prominent stress-strain hysteresis loop indicates significant strain partitioning and a back stress strengthening effect within the alloy [60]. As the deformation proceeds, the strain partitioning will lead to greater strain discordance between the soft and hard regions. However, the strain must remain continuous at the interfaces. Geometrically necessary dislocations will be formed to accommodate the strain gradient, which will generate greater back stresses within the soft regions, thus further increasing the ultimate strength. It is important to note that geometrically necessary dislocations resulting from strain partitioning between the soft and hard regions are responsible for the generation of strain gradients [48].

The schematic diagram of Fig. 11 compares the tensile property enhancement mechanism of homogeneous and heterogeneous structures. In the homogeneous structures (Fig. 11a-c), deformation initiates in the GB α phase region due to the lower strength of the GB α than the intragranular lamellar α region, causing strain localization and crack nucleation at GBs. Due to premature crack nucleation, it is difficult to induce deformation of the intragranular lamellar α phase, which eventually leads to crack propagation along the GBs and intergranular brittle

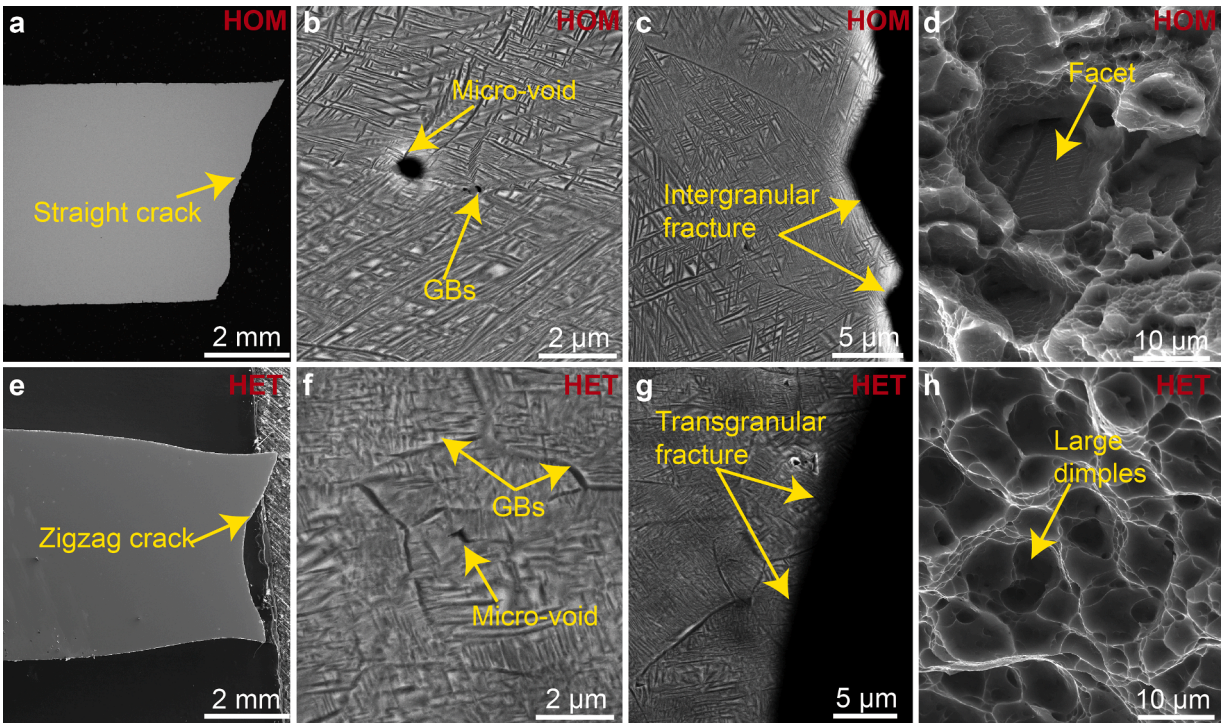

Fig. 9. Comparison of fracture mechanisms of homogeneous (a-d) (the same specimen as Fig. 6d) and heterogeneous structures (e-g) (the same specimen as Fig. 5d). (a) Macroscopic image near the fracture, straight fracture surface without obvious necking. (b) The micro-cracks nucleation at the GBs, resulting (c) the cracks propagate along the GBs. (d) The brittle fracture facet of homogeneous structures. (e) Macroscopic image near the fracture, tortuous crack with obvious necking. (f) Micro-cracks nucleate at intragranular coarse lamellar α region. (g) The cracks propagate within the β grain. (h) The large dimple of the heterostructures.

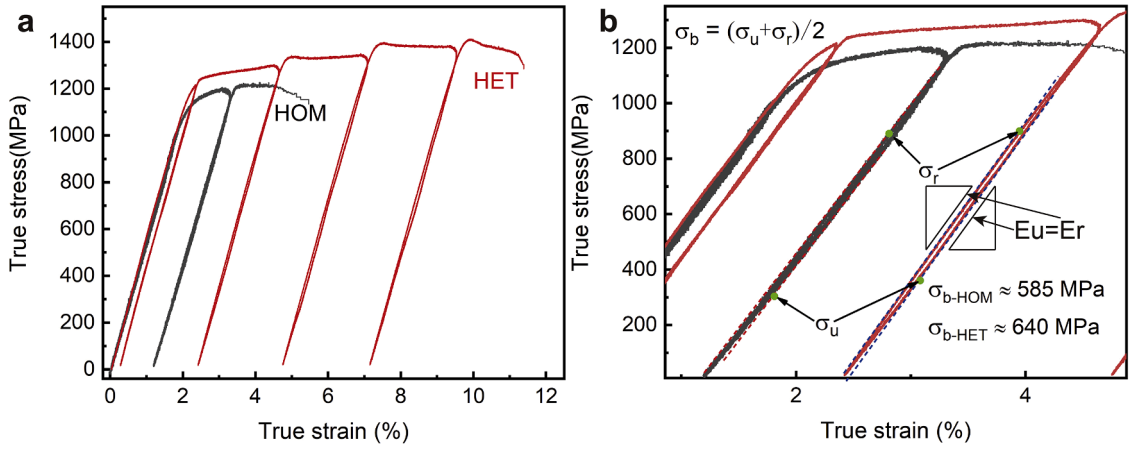

Fig. 10. Back stresses of the homogeneous and heterostructure alloys (the same specimen as Fig. 5d and 6d). (a) Cyclic loading and unloading experiments on the homogeneous and heterostructure samples. (b) The back stress σ_b is half of the unloading yield stress (σ_u) and reloading yield stress (σ_r). The back stresses are 585 MPa and 640 MPa for homogeneous and heterogeneous structure alloys, respectively.

fracture. In the heterostructures (Fig. 11d-f), the ultra-fine α phase at the GBs effectively strengthens the GBs, avoids strain localization at the GBs and stimulates the deformation of the coarse α phase. Subsequently, dislocations in the coarse α region glide to and are stopped by the interface region and form geometrically necessary dislocations, which not only further increase the deformation but also generate long-range back stresses in the coarse α region to reinforce the soft region. The strengthening of the soft region will further eliminate strain localization and stimulate continued deformation by dislocation and twinning in the hard region (ultra-fine α region) and, thus, increase strain hardening. Meanwhile, the nucleation and propagation of microcracks do not occur at GBs, but within the grains, leading to the tortuous transgranular ductile fractures.

4. Conclusion

In summary, our work presents a simple and effective method for designing heterostructures (heterogeneous precipitate microstructures) in the commercial Ti-55531 alloy to achieve a synergistic enhancement of strength and ductility. By exploiting solute redistribution upon up-quenching, which lags significantly behind the structural transformation, and guided by phase field simulations, we have demonstrated experimentally that micrometer-scale composition modulations can be created in a single β phase by up-quenching a pre-existing globular α_p + β microstructure. Such composition modulations activate different α precipitation mechanisms simultaneously and lead to spatially heterogeneous microstructures with alternating ultra-fine and coarse α

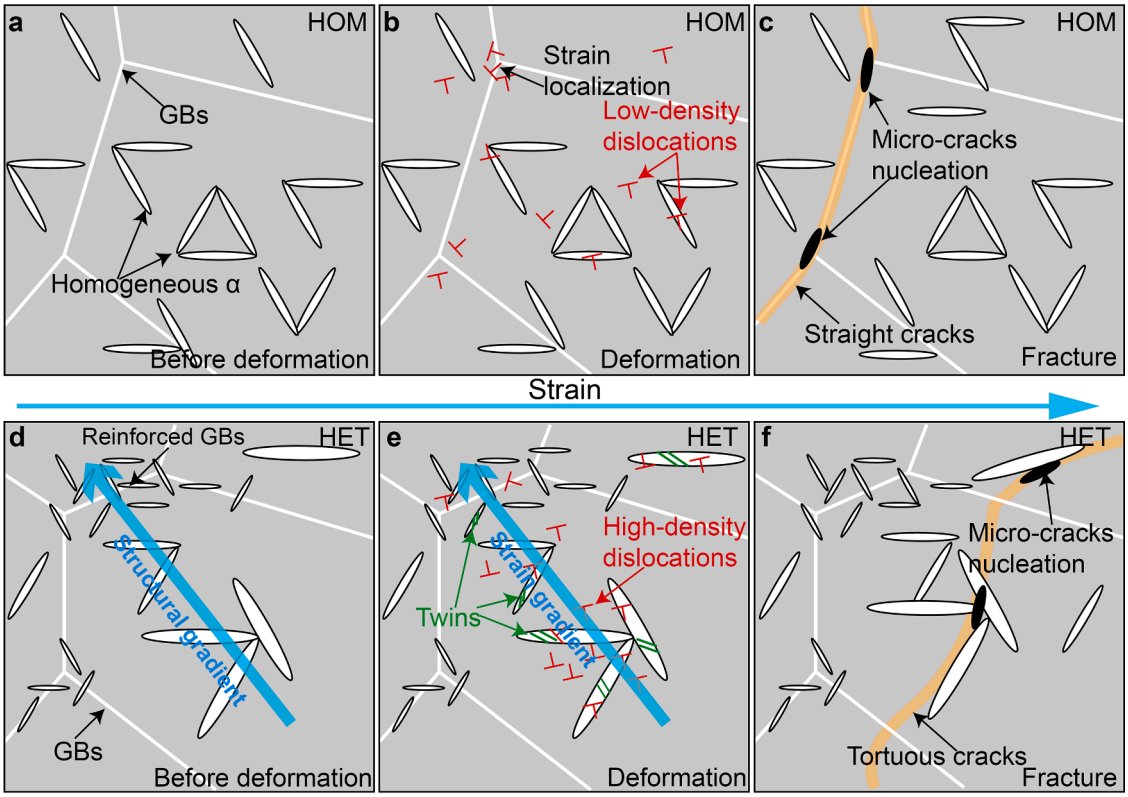

Fig. 11. Comparison of deformation and fracture modes of homogeneous (a-c) and heterogeneous structures (d-f). (a) Before deformation, uniform α phase is uniformly distributed in GBs and within grains. (b) The low strength of the GB α causes strain localization at the GBs, and the deformation mode of the homogeneous structure is low density of dislocations. (c) Micro-cracks nucleate at the GBs and propagate along the GBs, resulting in intergranular brittle fracture. (d) Before deformation, coarse and ultra-fine α phases form a structural gradient, and the ultra-fine α phase at the GBs effectively strengthens the GBs and avoids strain localization. (e) The strain gradient of heterostructure activates the deformation of the ultra-fine α phase and further avoids strain localization at GBs. The deformation modes of heterostructure are the high density of dislocations and deformation twinning in coarse and ultra-fine α phases. (f) Micro-cracks nucleate in the intragranular coarse α-phase region and propagate within the grain, resulting in ductile fracture.

precipitates, with the ultra-fine α regions primarily located at the prior β GBs. Experimental characterizations reveal that the globular α_p precipitates become α-stabilizer-rich phantom α_p (with a BCC structure) during the up-quenching heat treatment, where congruent structural transformation takes place followed by decomposition upon aging, leading to the formation of ultra-fine α precipitates. In the meantime, in the β-stabilizer-rich regions, α precipitation follows the classical nucleation-and-growth mechanism, yielding coarse α precipitates. Mechanical testing results indicate that the resulting heterostructured alloy exhibits significant enhancements in both ductility (by 130%) and ultimate strength (by 6%) over the homogeneous alloy counterpart. SEM and TEM characterizations reveal that the enhanced ductility of the heterostructured alloy could be attributed to its unique microstructure that avoids strain localization at prior β GBs, allowing deformation by dislocations and twinning continue in the coarse and ultra-fine α regions. The high strength of the alloy could be attributed to the significantly increased back stress effect caused by the strain partitioning in the heterogeneous precipitate microstructures. This work offers a simple and low-cost method readily implementable in industrial practices for achieving bulk heterostructures in precipitation-hardened alloys, leading to significant enhancement in both ductility and strength.

Data availability

The data that support the findings of this study are available from the corresponding author upon reasonable request.

Author contributions

L. L., D. Wang, and Y. W. conceived the idea and designed the research. D. Wu designed the experimental parameters, prepared the specimens and characterized the microstructure. M. H. performed phase field simulations. T. Z. performed some tensile property tests. D. Wu, T. Z., Z. W. and D. Wang analyzed the data and discussed the results. D. Wu, M. H., T. Z., L. L., D. Wang and Y. W. co-authored the manuscript. All authors discussed the results and commented on the manuscript.

Declaration of Competing Interest

The authors declare that they have no known competing financial interests or personal relationships that could have appeared to influence the work reported in this paper.

Acknowledgement

D. Wu, L. Z. and L. L. acknowledge the support by the National Natural Science Foundation of China (Grant No. 52071339, 51901251) and Scientific Research and Technology Development Program of Guangxi (Grant No. AD22035997), D. Wang acknowledges the support by the National Key Research and Development Program of China (Grant No. 2021YFB3702603) and the National Natural Science Foundation of China (Grant No. 51931004, 52171012), 111 project (BP2018008), the GHfund A (ghfund202302019461) and "H2" High-

Performance Cluster. G. R. and J. W. acknowledge the support by the Foundation for Guangxi Bagui scholars. Y. W. acknowledges the support by the US National Science Foundation (Grant No. DMR-1923929), which has facilitated this continued international collaboration.

Supplementary materials

Supplementary material associated with this article can be found, in the online version, at doi:10.1016/j.actamat.2023.119182.

References

[1] Z. Cheng, H. Zhou, Q. Lu, H. Gao, L. Lu, Extra strengthening and work hardening in gradient nanotwinned metals, Science 362 (2018) 1925–1934.
[2] Z. Li, K.G. Pradeep, Y. Deng, D. Raabe, C.C. Tasan, Metastable high-entropy dual-phase alloys overcome the strength–ductility trade-off, Nature 534 (2016) 227–230.
[3] X. Wang, R.R. De Vecchis, C. Li, H. Zhang, X. Hu, S. Sridar, Y. Wang, W. Chen, W. Xiong, Design metastability in high-entropy alloys by tailoring unstable fault energies, Sci. Adv. 8 (2022) eabo7333.
[4] L. Romero-Resendiz, M. El-Tahawy, T. Zhang, M.C. Rossi, D.M. Marulanda-Cardona, T. Yang, V. Amigó-Borrás, Y. Huang, H. Mirzadeh, I.J. Beyerlein, J. C. Huang, T.G. Langdon, Y.T. Zhu, Heterostructured stainless steel: Properties, current trends, and future perspectives, Mater. Sci. Eng. R Rep. 150 (2022), 100691.
[5] X.T. Fang, G.Z. He, C. Zheng, X.L. Ma, D. Kaoumi, Y.S. Li, Y.T. Zhu, Effect of heterostructure and hetero-deformation induced hardening on the strength and ductility of brass, Acta Mater. 186 (2020) 644–655.
[6] Y.F. Wang, M.S. Wang, X.T. Fang, F.J. Guo, H.Q. Liu, R.O. Scattergood, C.X. Huang, Y.T. Zhu, Extra strengthening in a coarse/ultrafine grained laminate: Role of gradient interfaces, Int. J. Plast. 123 (2019) 196–207.
[7] Y. Wang, Y. Wei, Z. Zhao, Z. Lin, F. Guo, Q. Cheng, C. Huang, Y. Zhu, Mechanical response of the constrained nanostructured layer in heterogeneous laminate, Scr. Mater. 207 (2022), 114310.
[8] X. Wu, Y. Zhu, K. Lu, Ductility and strain hardening in gradient and lamellar structured materials, Scr. Mater. 186 (2020) 321–325.
[9] T.H. Fang, W.L. Li, N.R. Tao, K. Lu, Revealing extraordinary intrinsic tensile plasticity in gradient nano-grained copper, Science 331 (2011) 1587–1590.
[10] C.X. Huang, Y.F. Wang, X.L. Ma, S. Yin, H.W. Höppel, M. Göken, X.L. Wu, H.J. Gao, Y.T. Zhu, Interface affected zone for optimal strength and ductility in heterogeneous laminate, Mater. Today 21 (2018) 713–719.
[11] H. Li, H. Zong, S. Li, S. Jin, Y. Chen, M.J. Cabral, B. Chen, Q. Huang, Y. Chen, Y. Ren, K. Yu, S. Han, X. Ding, G. Sha, J. Lian, X. Liao, E. Ma, J. Sun, Uniting tensile ductility with ultrahigh strength via composition undulation, Nature 604 (2022) 273–279.
[12] B. Sun, W. Lu, B. Gault, R. Ding, S.K. Makineni, D. Wan, C.H. Wu, H. Chen, D. Ponge, D. Raabe, Chemical heterogeneity enhances hydrogen resistance in high-strength steels, Nat. Mater. 20 (2021) 1629–1634.
[13] S.K. Vajpai, C. Sawangrat, O. Yamaguchi, O.P. Ciuca, K. Ameyama, Effect of bimodal harmonic structure design on the deformation behaviour and mechanical properties of Co-Cr-Mo alloy, Mater. Sci. Eng. C 58 (2016) 1008–1015.
[14] R. Zheng, Z. Zhang, M. Nakatani, M. Ota, X. Chen, C. Ma, K. Ameyama, Enhanced ductility in harmonic structure designed SUS316L produced by high energy ball milling and hot isostatic sintering, Mater. Sci. Eng. A Struct. Mater. 674 (2016) 212–220.
[15] B. Gao, Q. Lai, Y. Cao, R. Hu, L. Xiao, Z. Pan, N. Liang, Y. Li, S. Gang, M. Liu, H. Zhou, X. Wu, Y. Zhu, Ultrastrong low-carbon nanosteel produced by heterostructure and interstitial mediated warm rolling, Sci. Adv. 6 (2020) 8169–8192.
[16] Y. Zhu, X. Wu, Heterostructured materials, Prog. Mater Sci. 131 (2023), 101019.
[17] D. Banerjee, J.C. Williams, Perspectives on Titanium Science and Technology, Acta Mater. 61 (2013) 844–879.
[18] Y. Zheng, R.E.A. Williams, G.B. Viswanathan, W.A.T. Clark, H.L. Fraser, Determination of the structure of α-β interfaces in metastable β-Ti alloys, Acta Mater. 150 (2018) 25–39.
[19] C. Huang, Y. Zhao, S. Xin, W. Zhou, Q. Li, W. Zeng, Effect of microstructure on tensile properties of Ti–5Al–5Mo–5V–3Cr–1Zr alloy, J. Alloy. Compd. 693 (2017) 582–591.
[20] S. Nag, R. Banerjee, R. Srinivasan, J.Y. Hwang, M. Harper, H.L. Fraser, ω-Assisted nucleation and growth of α precipitates in the Ti–5Al–5Mo–5V–3Cr–0.5Fe β titanium alloy, Acta Mater. 57 (2009) 2136–2147.
[21] N.G. Jones, R.J. Dashwood, M. Jackson, D. Dye, β Phase decomposition in Ti–5Al–5Mo–5V–3Cr, Acta Mater. 57 (2009) 3830–3839.
[22] S. Nag, Y. Zheng, R.E.A. Williams, A. Devaraj, A. Boyne, Y. Wang, P.C. Collins, G. B. Viswanathan, J.S. Tiley, B.C. Muddle, R. Banerjee, H.L. Fraser, Non-classical homogeneous precipitation mediated by compositional fluctuations in titanium alloys, Acta Mater. 60 (2012) 6247–6256.
[23] T. Zhang, D. Wang, J. Zhu, H. Xiao, C.T. Liu, Y. Wang, Non-conventional transformation pathways and ultrafine lamellar structures in γ-TiAl alloys, Acta Mater. 189 (2020) 25–34.
[24] R. Shi, V. Dixit, H.L. Fraser, Y. Wang, Variant selection of grain boundary α by special prior β grain boundaries in titanium alloys, Acta Mater. 75 (2014) 156–166.
[25] T. Takaki, M. Ohno, T. Shimokawabe, T. Aoki, Two-dimensional phase-field simulations of dendrite competitive growth during the directional solidification of a binary alloy bicrystal, Acta Mater. 81 (2014) 272–283.
[26] A. Boyne, D. Wang, R.P. Shi, Y. Zheng, A. Behera, S. Nag, J.S. Tiley, H.L. Fraser, R. Banerjee, Y. Wang, Pseudospinodal mechanism for fine α/β microstructures in β-Ti alloys, Acta Mater. 64 (2014) 188–197.
[27] D. Wang, Q. Liang, S. Zhao, P. Zhao, T. Zhang, L. Cui, Y. Wang, Phase field simulation of martensitic transformation in pre-strained nanocomposite shape memory alloys, Acta Mater. 164 (2019) 99–109.
[28] U. Grafe, B. Böttger, J. Tiaden, S.G. Fries, Coupling of multicomponent thermodynamic databases to a phase field model: application to solidification and solid state transformations of superalloys, Scr. Mater. 42 (2000) 1179–1186.
[29] Y. Ni, W. Rao, A.G. Khachaturyan, Pseudospinodal mode of decomposition in films and formation of chessboard-like nanostructure, Nano Lett. 9 (2009) 3275–3281.
[30] T. Zhou, M. Aindow, S.P. Alpay, M.J. Blackburn, M.H. Wu, Pseudo-elastic deformation behavior in a Ti/Mo-based alloy, Scr. Mater. 50 (2004) 343–348.
[31] M. Hao, P. Li, L. Xuexiong, Z. Tianlong, D. Wang, Q. Sun, L. Liu, J. Li, Y. Cui, R. Yang, D. Xu, Heterogeneous precipitate microstructure in titanium alloys for simultaneous improvement of strength and ductility, J. Mater. Sci. Technol. 124 (2022) 150–163.
[32] P. Guo, Y. Zhao, W. Zeng, Q. Hong, The effect of microstructure on the mechanical properties of TC4-DT titanium alloys, Mater. Sci. Eng. A 563 (2013) 106–111.
[33] O.M. Ivasishin, P.E. Markovsky, Yu.V. Matviychuk, S.L. Semiatin, C.H. Ward, S. Fox, A comparative study of the mechanical properties of high-strength β-titanium alloys, J. Alloy. Compd. 457 (2008) 296–309.
[34] A. Ghosh, S. Sivaprasad, A. Bhattacharjee, S.K. Kar, Microstructure–fracture toughness correlation in an aircraft structural component alloy Ti–5Al–5V–5Mo–3Cr, Mater. Sci. Eng. A, 568 (2013) 61–67.
[35] S.L. Nyakana, J.C. Fanning, R.R. Boyer, Quick reference guide for β titanium alloys in the 00 s, J. Mater. Eng. Perform. 14 (2005) 799–811.
[36] G. Srinivasu, Y. Natraj, A. Bhattacharjee, T.K. Nandy, G.V.S. Nageswara Rao, Tensile and fracture toughness of high strength β Titanium alloy, Ti–10V–2Fe–3Al, as a function of rolling and solution treatment temperatures, Mater. Des. 47 (2013) 323–330.
[37] G.T. Terlinde, T.W. Duerig, J.C. Williams, Microstructure, tensile deformation, and fracture in aged ti 10V-2Fe-3Al, MTA 14 (1983) 2101–2115.
[38] S.L. Raghunathan, R.J. Dashwood, M. Jackson, S.C. Vogel, D. Dye, The evolution of microtexture and macrotexture during subtransus forging of Ti–10V–2Fe–3Al, Mater. Sci. Eng. A, 488 (2008) 8–15.
[39] Pei Li, Qiaoyan Sun, Lin Xiao, Jun Sun, Tuning the morphology of Ti–5Al–5Mo–5V–3Cr–1Zr alloy: From brittle to ductile fracture, Adv. Top. Mater. Sci. Eng. A, 769 (2020) 138487–138495.
[40] D. Qin, Y. Lu, Q. Liu, L. Zheng, L. Zhou, Transgranular shearing introduced brittlement of Ti–5Al–5V–5Mo–3Cr alloy with full lamellar structure at room temperature, Mater. Sci. Eng. A, 572 (2013) 19–24.
[41] D. Wu, L. Liu, L. Zeng, W. Zhu, W. Wang, X. Zhang, J. Hou, B. Liu, J. Lei, K. Zhou, Designing high-strength titanium alloy using pseudo-spinodal mechanism through diffusion multiple experiment and CALPHAD calculation, J. Mater. Sci. Technol. 74 (2021) 78–88.
[42] Y. Chen, Z. Du, S. Xiao, L. Xu, J. Tian, Effect of aging heat treatment on microstructure and tensile properties of a new β high strength titanium alloy, J. Alloy. Compd. 586 (2014) 588–592.
[43] K.C. Chen, W.W. Wu, C.N. Liao, L.J. Chen, K.N. Tu, Observation of atomic diffusion at twin-modified grain boundaries in copper, Science 321 (2008) 1066–1069.
[44] X. Li, Y. Wei, L. Lu, K. Lu, H. Gao, Dislocation nucleation governed softening and maximum strength in nano-twinned metals, Nature 464 (2010) 877–880.
[45] H.Y. Hsiao, C.M. Liu, H. Lin, T.C. Liu, C.L. Lu, Y.S. Huang, C. Chen, K.N. Tu, Unidirectional growth of microbumps on (111)-oriented and nanotwinned copper, Science 336 (2012) 1007–1010.
[46] P. Zhao, C. Shen, M.F. Savage, J. Li, S.R. Niezgoda, M.J. Mills, Y. Wang, Slip transmission assisted by Shockley partials across α/β interfaces in Ti-alloys, Acta Mater. 171 (2019) 291–305.
[47] X. Wu, Y. Zhu, Gradient and lamellar heterostructures for superior mechanical properties, MRS Bull. 46 (2021) 244–249.
[48] Y. Zhu, X. Wu, Perspective on hetero-deformation induced (HDI) hardening and back stress, Mater. Res. Lett. 7 (2019) 393–398.
[49] E. Clouet, D. Caillard, N. Chaari, F. Onimus, D. Rodney, Dislocation locking versus easy glide in titanium and zirconium, Nature Mater. 14 (2015) 931–936.
[50] M. Ahmed, D. Wexler, G. Casillas, D.G. Savvakin, E.V. Pereloma, Strain rate dependence of deformation-induced transformation and twinning in a metastable titanium alloy, Acta Mater. 104 (2016) 190–200.
[51] D. Wu, L. Liu, L. Zhang, W. Wang, K. Zhou, Tensile deformation mechanism and micro-void nucleation of Ti-55531 alloy with bimodal microstructure, J. Mater. Res. Technol. 9 (2020) 15442–15453.
[52] W. Zhu, Q. Sun, C. Tan, P. Li, L. Xiao, J. Sun, Tensile brittleness and ductility improvement in a novel metastable β titanium alloy with lamella structure, J. Alloy. Compd. 827 (2020), 154311.
[53] S. Xu, M. Gong, Y. Jiang, C. Schuman, J.S. Lecomte, J. Wang, Secondary twin variant selection in four types of double twins in titanium, Acta Mater. 152 (2018) 58–76.
[54] A. Ghaderi, M.R. Barnett, Sensitivity of deformation twinning to grain size in titanium and magnesium, Acta Mater. 59 (2011) 7824–7839.
[55] Z. Guo, A.P. Miodownik, N. Saunders, J.Ph. Schillé, Influence of stacking-fault energy on high temperature creep of alpha titanium alloys, Scr. Mater. 54 (2006) 2175–2178.

[56] A. Fitzner, D.G.L. Prakash, J.Q. da Fonseca, M. Thomas, S.Y. Zhang, J. Kelleher, P. Manuel, M. Preuss, The effect of aluminium on twinning in binary alpha-titanium, Acta Mater. 103 (2016) 341–351.
[57] J.G. Gibeling, W.D. Nix, A numerical study of long range internal stresses associated with subgrain boundaries, Acta Metall. 28 (1980) 1743–1752.
[58] M. Yang, Y. Pan, F. Yuan, Y. Zhu, X. Wu, Back stress strengthening and strain hardening in gradient structure, Mater. Res. Lett. 4 (2016) 145–151.
[59] S. Cw, E. Jd, Role of internal stresses in co-deformed two-phase materials, Philos. Mag. 86 (2006) 4081–4098.
[60] Y. Zhou, K. Wang, X. Wen, R. Xin, J. Wang, Q. Liu, Achieving synergy enhancement of strength and ductility in Ti-6Al-2Sn-4Zr-2Mo-0.1Si alloy by fabricating a new multiscale microstructure, Scr. Mater. (2023) 115233–115237.